(Received 5 December 2025, Accepted 21 February 2026, Scheduled 8 April 2026)

Vibration Suppression of Bearingless Interior Permanent Magnet Synchronous Motor Based on Improved Repetitive Controller

Bo Yue, Yizhou Hua*, and Huangqiu Zhu

School of Electrical and Information Engineering, Jiangsu University, Zhenjiang 212013, China

ABSTRACT: Bearingless interior permanent magnet synchronous motors (BIPMSMs) have a simpler and more compact structure and incur a lower cost than motors supported by magnetic bearings. BIPMSMs offer the advantages of both magnetic bearings and conventional interior permanent magnet synchronous motors. However, rotor vibrations can severely degrade the performance and limit the application of BIPMSMs. Therefore, vibration suppression in BIPMSMs is investigated in this study. First, the factors causing rotor vibrations are analyzed, and the mathematical model of the unbalanced force that causes rotor vibrations is derived in terms of the rotor mass unbalance and inverter dead-time effect. Second, a vibration suppression strategy based on a variable sampling frequency repetitive controller is proposed to enable stable motor operation over a wide frequency range. The sampling frequency is dynamically adjusted according to the change in the vibration frequency to maintain a constant order of the repetitive controller. Finally, simulations and experiments are conducted to verify the effectiveness of the proposed vibration suppression strategy.

1. INTRODUCTION

Bearingless interior permanent magnet synchronous motors (BIPMSMs) contain an additional set of suspension force windings embedded in the stator to achieve stable rotor suspension, thereby combining the magnetic suspension technology with conventional interior permanent magnet synchronous motors. They retain the advantages of magnetic bearings that require no lubrication, exhibit no mechanical wear, and have a long service life. They also offer the benefits of interior permanent magnet synchronous motors, such as high efficiency and power density. Furthermore, this integration yields a more compact structure and lower cost than the motors supported by magnetic bearings [1–3]. BIPMSMs have been widely adopted in high-speed, high-precision, and clean applications owing to these characteristics [4]. However, problems such as unbalanced rotor mass and mechanical assembly accuracy cause excitation forces at the same frequency as that of the rotational speed during rotor rotation. It leads to rotor vibrations, which severely limit the performance, application, and safety of BIPMSMs. Therefore, the research on vibration suppression in BIPMSMs is crucial.

Extensive research has been conducted on suppressing rotor vibrations in bearingless motors [5–9]. In [5], an unbalanced vibration suppression control was proposed based on an improved total least square algorithm. The logarithmic function was introduced to enhance its cost function, thereby further improving the anti-disturbance performance of the algorithm. In [6], an unbalanced force feedforward compensation controller was designed to extract the synchronous vibration signals using a synchronous signal detection unit and then generate the compensating force components through the unbalanced feedforward compensation controller. In [7], an unbalanced vibration suppression control method was proposed based on variable step size and angle search algorithms; a fuzzy inference system was employed to adjust the function weights, and a vibration suppression control system was constructed accordingly. In [8], a phase shift notch filter combined with feed-forward control was employed to individually eliminate the vibration forces caused by current stiffness and displacement stiffness. In [9], system stability was achieved across the entire speed range by adjusting the phase angle, and residual synchronous vibration forces due to negative displacement stiffness were eliminated by compensating for the phase lag effect of the power amplifier. However, the algorithms of these control methods are complex and computationally intensive, which can cause computational delays at high rotational speeds, thereby limiting the response speed and stability of the control system. Furthermore, these studies only considered the rotor vibrations caused by rotor mass imbalance, and limited research was conducted on vibrations caused by other factors.

Rotor vibrations are also caused by the dead-time effect of the inverter. Dead-time is introduced to prevent the simultaneous conduction of the upper and lower arms of the inverter, which causes a short circuit. However, this leads to voltage loss and waveform distortion, which result in periodic unbalanced forces in the motor [10]. Repetitive control based on the internal model principle involves periodic accumulation of error correction and infinite gain at the fundamental and harmonic frequencies of the system. This enables zero steady-state error

* Corresponding author: Yizhou Hua (huayz@ujs.edu.cn).

tracking of periodic signals and effective suppression [11, 12], which simultaneously suppress the rotor vibrations caused by both the rotor mass imbalance and dead-time effect. The conventional implementation method for variable-speed repetitive controllers is the fractional-order delay approach. In [13], a fractional-order delay repetitive control algorithm was adopted to maintain the performance of the repetitive controller under a fixed sampling frequency. This method offers advantages such as convenient parameter adjustment and fast dynamic response. However, in application scenarios with a wide range of variable frequencies, the feasibility and optimal design of the fractional-order delay repetitive control remain a major challenge.

The rotor vibration mechanism in BIPMSMs is comprehensively investigated in this study. The vibrations caused by the rotor mass imbalance and dead-time effect are analyzed, and a mathematical model of the unbalanced force is established. A variable-speed repetitive controller based on the variable sampling frequency method is proposed to suppress rotor vibrations at different frequencies in BIPMSMs. The sampling frequency is maintained as a fixed multiple of the vibration frequency by configuring the pulse width modulation (PWM) to trigger sampling and cyclically updating the PWM period value. Thus, the order of the delay element in the repetitive controller remains constant. Compared with the fractional-order delay repetitive controller, the proposed method exhibits greater robustness and better dynamic performance. Furthermore, compared with the existing vibration suppression strategies, it incurs less computational overhead and eliminates the need for complex parallel or cascade structures, thereby significantly reducing the design complexity.

A vibration suppression control strategy based on a variable sampling frequency repetitive controller is proposed in this study to enable the stable operation of BIPMSMs over a wide frequency range. The remainder of this paper is organized as follows. Section 2 introduces the operational principles and mathematical model of the BIPMSM and an analysis of the vibration mechanisms. Section 3 presents the fundamental theory of repetitive control and a variable-speed repetitive controller designed using the variable sampling frequency method. Section 4 describes the verification of the effectiveness of the proposed vibration suppression strategy through simulations and experiments, and Section 5 summarizes the study.

2. MATHEMATICAL MODEL AND VIBRATION ANALYSIS

2.1. Mathematical Model of BIPMSMs

BIPMSMs comprise two sets of windings: torque winding and suspension force winding, and their pole pair numbers differ by 1, as shown in Fig. 1. The case where the torque winding has one pole pair, and the suspension force winding has two pole pairs is taken as an example: I_{T} and I_{S} in Fig. 1 represent the currents in the torque winding and suspension force winding, respectively. The magnetomotive force (MMF) decreases when the MMFs generated by the suspension force winding and torque winding are in opposite directions. Conversely, the MMF increases when the MMFs produced by the two windings

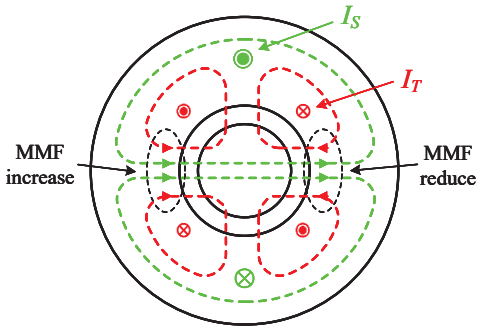

FIGURE 1. Mechanism of suspension force generation.

are in the same direction. Therefore, a radial force is generated along the direction in which the MMF increases.

As per the virtual displacement theory [14], the radial suspension force acting on the rotor of the BIPMSM can be derived by constructing the inductance matrix, calculating the magnetic co-energy W_{m}, and then obtaining the partial derivative with respect to the radial displacement. The suspension force components on the rotor in the direct-quadrature (d-q) axis reference frame are given as follows:

$$\begin{bmatrix} F_{\mathrm{Sd}} \\ F_{\mathrm{Sq}} \end{bmatrix} = \begin{bmatrix} M_{\mathrm{d}}(i_{\mathrm{Td}} + i_{\mathrm{f}}) & M_{\mathrm{q}} i_{\mathrm{Tq}} \\ M_{\mathrm{q}} i_{\mathrm{Tq}} & -M_{\mathrm{d}}(i_{\mathrm{Td}} + i_{\mathrm{f}}) \end{bmatrix} \begin{bmatrix} i_{\mathrm{Sd}} \\ i_{\mathrm{Sq}} \end{bmatrix} \tag{1}$$

where i_{Td} and i_{Tq} represent the current components of the torque winding in the d-q reference frame; i_{Sd} and i_{Sq} represent the current components of the suspension force winding in the d-q reference frame; i_{f} represents the equivalent excitation current of the permanent magnet; and M_{d} and M_{q} represent the mutual inductance components between the torque winding and suspension force winding in the d-q reference frame.

The suspension force of the BIPMSM in the α-β stationary reference frame can be derived as follows:

$$\begin{bmatrix} F_{\mathrm{S}\alpha} \\ F_{\mathrm{S}\beta} \end{bmatrix} = \sqrt{M_{\mathrm{d}}^2 (i_{\mathrm{Td}} + i_{\mathrm{f}})^2 + M_{\mathrm{q}}^2 i_{\mathrm{Tq}}^2} \times \begin{bmatrix} -\cos(2\omega_{\mathrm{m}} t + \theta) & \sin(2\omega_{\mathrm{m}} t + \theta) \\ \sin(2\omega_{\mathrm{m}} t + \theta) & \cos(2\omega_{\mathrm{m}} t + \theta) \end{bmatrix} \begin{bmatrix} i_{\mathrm{S}\alpha} \\ i_{\mathrm{S}\beta} \end{bmatrix} \tag{2}$$

where ω_{m} represents the mechanical angular velocity of the rotor.

In the BIPMSM, the interior permanent magnet rotor is subjected to an unbalanced magnetic force component, along with the controllable suspension force, when an eccentric displacement occurs. The unbalanced force is proportional to the rotor eccentric displacement, and its proportionality coefficient is proportional to the square of the torque winding current. In the stationary coordinate system, the unbalanced force can be expressed as follows:

$$\begin{bmatrix} F_{\mathrm{c}\alpha} \\ F_{\mathrm{c}\beta} \end{bmatrix} = \left[k_{\mathrm{d}} (i_{\mathrm{Td}} + i_{\mathrm{f}})^2 + k_{\mathrm{q}} i_{\mathrm{Tq}}^2 \right] \begin{bmatrix} x \\ y \end{bmatrix} \tag{3}$$

where k_{d} and k_{q} represent the proportional factors, and x and y are the components of the rotor displacement in the α-β stationary reference frame.

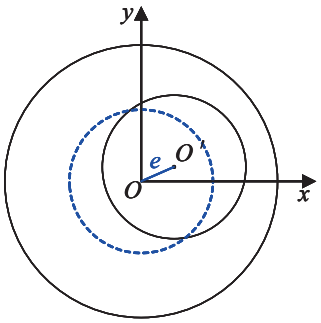

FIGURE 2. Mechanism of rotor vibration.

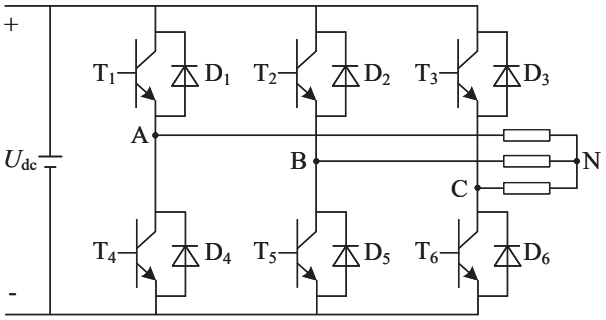

FIGURE 3. Topology of the inverter.

Therefore, the complete mathematical model of the suspension force in the BIPMSM can be established by considering both the controllable suspension force generated by the suspension force winding and the unbalanced magnetic force due to rotor eccentricity. It is expressed as follows:

$$\begin{bmatrix} F_\alpha \\ F_\beta \end{bmatrix} = \sqrt{M_{\mathrm{d}}^2 (i_{\mathrm{Td}} + i_{\mathrm{f}})^2 + M_{\mathrm{q}}^2 i_{\mathrm{Tq}}^2} \times \begin{bmatrix} -\cos(2\omega_{\mathrm{m}} t + \theta) & \sin(2\omega_{\mathrm{m}} t + \theta) \\ \sin(2\omega_{\mathrm{m}} t + \theta) & \cos(2\omega_{\mathrm{m}} t + \theta) \end{bmatrix} \begin{bmatrix} i_{S\alpha} \\ i_{S\beta} \end{bmatrix} + \left[k_{\mathrm{d}} (i_{\mathrm{Td}} + i_{\mathrm{f}})^2 + k_{\mathrm{q}} i_{\mathrm{Tq}}^2 \right] \begin{bmatrix} x \\ y \end{bmatrix} \tag{4}$$

2.2. Vibration Analysis for BIPMSMs

During the manufacturing process of BIPMSMs, factors such as machining errors and assembly inaccuracies cause the rotor's center of mass O' to deviate from its geometric center O, resulting in an eccentricity e, as illustrated in Fig. 2. During the operation, due to centrifugal effects, the rotor is subjected to a centrifugal force, F_a, which increases with the rotational speed owing to centrifugal effects. Its components in the stationary coordinate system are:

$$\begin{bmatrix} F_{ax} \\ F_{ay} \end{bmatrix} = me\omega_{\mathrm{m}}^2 \begin{bmatrix} \cos(\omega_{\mathrm{m}} t + \eta) \\ \sin(\omega_{\mathrm{m}} t + \eta) \end{bmatrix} \tag{5}$$

where F_{ax} and F_{ay} represent the components of the unbalanced force on the x-axis and y-axis, respectively.

According to (5), the unbalanced displacement varies periodically with a period of $2\pi/\omega_m$.

The unbalanced force generated during the BIPMSM operation is influenced by both motor manufacturing tolerances and the control process, with the dead-time effect being the most direct cause. This effect originates from the inclusion of dead time, which is essential for preventing shoot-through faults across the upper and lower inverter arms. However, it causes the output voltage during dead-time periods to depend on the load current direction, leading to output waveform distortion, increased harmonics, and current steady-state error [15].

A three-phase voltage-source two-level inverter bridge is used in this study. Its topology is shown in Fig. 3, and the switching strategy involves Space Vector Pulse Width Modulation (SVPWM). The A-phase bridge is taken as an example: after dead time is introduced, the turn-on of T_1 is delayed. When the current direction is positive, and the power switch T_1 is in the turn-off process, the current briefly freewheels through D_4 during this period, whereas T_4 remains completely off. This causes the actual voltage to deviate from the ideal voltage across the power switching devices.

When the current direction remains unchanged, the voltage variation caused by the dead-time effect within a unit PWM cycle is:

$$\Delta u_{\mathrm{dead}} = (u_{\mathrm{dc}} + u_{\mathrm{D}} - u_{\mathrm{sw}}) \frac{T_{\mathrm{dead}}}{T_{\mathrm{PWM}}} + \frac{u_{\mathrm{sw}} + u_{\mathrm{D}}}{2} \tag{6}$$

where u_{dc} represents the DC bus voltage; u_{sw} represents the conduction voltage drop of the switching device; u_{D} represents the conduction voltage drop of the freewheeling diode; T_{dead} represents the dead time; and T_{PWM} represents the switching period.

For a BIPMSM operating without a flux-weakening control algorithm, the primary component of the Fourier series of this voltage can be analyzed after mapping the phase voltage variation caused by the dead-time voltage to the two-phase rotating coordinate system through Clarke and Park transformations. When the higher-order terms of the Fourier series are disregarded, it can be expressed as [16]:

$$\begin{bmatrix} \Delta u_{\mathrm{d}} \\ \Delta u_{\mathrm{q}} \end{bmatrix} = \frac{4}{\pi} \Delta u_{\mathrm{dead}} \begin{bmatrix} \frac{12}{35} \sin(6\theta_{\mathrm{e}}) + \frac{24}{143} \sin(12\theta_{\mathrm{e}}) \\ -1 + \frac{2}{35} \cos(6\theta_{\mathrm{e}}) - \frac{2}{143} \cos(12\theta_{\mathrm{e}}) \end{bmatrix} \tag{7}$$

where θ_e represents the rotor electrical angle.

When the motor is considered as a resistive and inductive load, the d-q axis currents can be expressed as:

$$\begin{bmatrix} \Delta i_d \\ \Delta i_q \end{bmatrix} = -\frac{4\Delta u_{\mathrm{dead}}}{\pi} \times \begin{bmatrix} \frac{12\sin(6\theta_{\mathrm{e}} - \phi_{\mathrm{d6}})}{35 Z_{\mathrm{d6}}} + \frac{24\sin(12\theta_{\mathrm{e}} - \phi_{\mathrm{d12}})}{143 Z_{\mathrm{d12}}} \\ -\frac{1}{R} + \frac{2\cos(6\theta_{\mathrm{e}} - \phi_{\mathrm{q6}})}{35 Z_{\mathrm{q6}}} - \frac{2\cos(12\theta_{\mathrm{e}} - \phi_{\mathrm{q12}})}{143 Z_{\mathrm{q12}}} \end{bmatrix} \tag{8}$$

where the impedance and phase angle are respectively:

$$\begin{cases} Z_{jk} = \sqrt{R_{\mathrm{s}}^2 + (k\omega_{\mathrm{e}} L_j)^2}, & j = d, q \\ \phi_{jk} = \arctan\left(\dfrac{k\omega_{\mathrm{e}} L_j}{R_{\mathrm{s}}}\right), & k = 6 \end{cases} \tag{9}$$

where R_{s} represents the rotor resistance of the motor; L_j represents the coil inductance; and ω_{e} represents the electrical angular velocity.

For the BIPMSM, (8) represents the current increments by Δi_{Td} and Δi_{Tq} in the d-q axis of the torque winding and the current increments by Δi_{Sd} and Δi_{Sq} in the d-q axis of the suspension-force winding. The expressions for the increments in the controllable suspension force in the x- and y-axis directions can be expressed as follows:

$$\begin{bmatrix} \Delta F_x \\ \Delta F_y \end{bmatrix} = \begin{bmatrix} M_{\mathrm{d}}(\Delta i_{\mathrm{Td}} + i_{\mathrm{f}}) & M_{\mathrm{q}} \Delta i_{\mathrm{Tq}} \\ M_{\mathrm{q}} \Delta i_{\mathrm{Tq}} & -M_{\mathrm{d}}(\Delta i_{\mathrm{Td}} + i_{\mathrm{f}}) \end{bmatrix} \begin{bmatrix} \Delta i_{\mathrm{Sd}} \\ \Delta i_{\mathrm{Sq}} \end{bmatrix} \tag{10}$$

where

$$\begin{bmatrix} \Delta i_{Td} \\ \Delta i_{Tq} \end{bmatrix} = \frac{4}{\pi} \Delta u_{\mathrm{dead}} \times \begin{bmatrix} \dfrac{12\sin(6\theta_e - \varphi_{Td6})}{35 Z_{Td6}} + \dfrac{24\sin(12\theta_e - \varphi_{Td12})}{143 Z_{Td12}} \\ \dfrac{1}{R_s} + \dfrac{2\cos(6\theta_e - \varphi_{Tq6})}{35 Z_{Tq6}} - \dfrac{2\cos(12\theta_e - \varphi_{Tq12})}{143 Z_{Tq12}} \end{bmatrix} \tag{11}$$

$$\begin{bmatrix} \Delta i_{Sd} \\ \Delta i_{Sq} \end{bmatrix} = \frac{4}{\pi} \Delta u_{\mathrm{dead}} \times \begin{bmatrix} \dfrac{12\sin(6\theta_e - \varphi_{Sd6})}{35 Z_{Sd6}} + \dfrac{24\sin(12\theta_e - \varphi_{Sd12})}{143 Z_{Sd12}} \\ \dfrac{1}{R_s} + \dfrac{2\cos(6\theta_e - \varphi_{Sq6})}{35 Z_{Sq6}} - \dfrac{2\cos(12\theta_e - \varphi_{Sq12})}{143 Z_{Sq12}} \end{bmatrix} \tag{12}$$

Substituting the motor parameters into (10) yields the harmonic order plot of the suspension force increment. This result is compared with that obtained under actual operating conditions, as shown in Fig. 4. As can been seen in (7), the amplitude of the 6th harmonic is the main influencing factor, and the waveform tested in practice remains consistent with the theoretical analysis. However, the theoretical amplitude of the 12th harmonic is considerably small, and a difference is observed between the 12th harmonic and the theoretical value in the actual working condition. This may correspond to the unmodeled nonlinear factor of the inverter. Therefore, in practice, the harmonic order of the force caused by the dead-time effect is mainly the 6th and 12th.

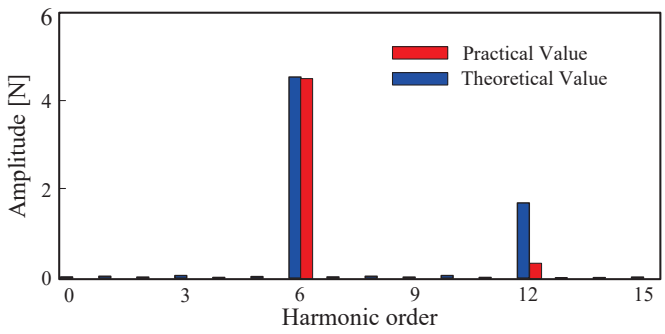

FIGURE 4. Harmonic analysis of vibration force.

In addition, the dead-time effect introduces switching ringing. The switching ringing injects high-frequency attenuated signals into the current, leading to suspension force fluctuations, which in turn excite rotor vibrations. It also contaminates current sampling and degrades the performance of the feedback loop. The influence of switching ringing is typically mitigated from a hardware perspective [17, 18], and it does not affect the conclusion that the 6th and 12th harmonics are the dominant harmonic components.

Superimposing the rotor vibrations caused by the rotor mass unbalance and dead-time effect shows that the resulting rotor vibrations are periodic with a frequency of f_v. Based on this vibration frequency, a repetitive controller can be designed to simultaneously suppress the vibrations caused by both factors.

3. VIBRATION SUPPRESSION STRATEGY BASED ON VARIABLE SPEED REPETITIVE CONTROLLER

3.1. Repetitive Control Principle

According to the internal model principle [19], for periodic input signals and disturbance signals, zero steady-state error can be achieved in tracking, and periodic signals can be rejected by incorporating a generator of the known periodic signal within a stable closed-loop system. Its internal model transfer function can be expressed as:

$$G_c(s) = \frac{e^{-Ts}}{1 - e^{-Ts}} \tag{13}$$

where T is the fundamental period of the signal.

Implementing the time-delay element e^{-Ts} in the repetitive controller within an analog system is difficult. In practical engineering applications, a digital implementation is adopted, and its transfer function in discrete form can be expressed as:

$$G_c(z) = \frac{z^{-N}}{1 - z^{-N}} \tag{14}$$

where N represents the number of samples per fundamental period.

When the input and disturbance signals are periodic with the fundamental period, the periodic accumulation of signals is enabled through the combined action of the periodic time-delay function z^{-N} and the positive feedback loop. Even when the input signal becomes zero, the controller continues to periodically output the same signal as that in the previous cycle. The periodic accumulation of the error signal is enabled by placing the repetitive controller in the forward path of the closed-loop control system. As long as a difference exists between the feedback value and reference value, the controller output amplitude continuously increases until the error is eliminated, and the feedback matches the reference. This ensures zero-error tracking in the steady state.

3.2. Design of the Repetitive Controller

Both (13) and (14) represent ideal repetitive controllers. These controllers can perfectly track the input signal and achieve a system characteristic with zero steady-state error. However, the control system contains N open-loop poles on the unit circle; thus, the system remains in a critically stable state. When system parameters or the controlled plant changes, the closed-loop control system becoming unstable is highly probable. Therefore, the stability and robustness of this ideal repetitive controller are relatively poor [20].

Currently, most practical application systems enhance the system stability by incorporating an internal model function $Q(z)$, thereby sacrificing some of the zero steady-state error characteristics. $Q(z)$ is typically selected as a constant slightly less than 1 or as a low-pass filter. In this case, Q is selected as a constant to simplify the design. The repetitive control transfer function can be expressed as:

$$G_c(z) = \frac{Qz^{-N}}{1 - Qz^{-N}} \tag{15}$$

The magnitude-frequency characteristics of the repetitive controller with different values of Q are compared in Fig. 5. The gain at the resonant frequency improves significantly with an increase in Q. To achieve higher gains while maintaining a sufficient stability margin, Q is set to 0.98.

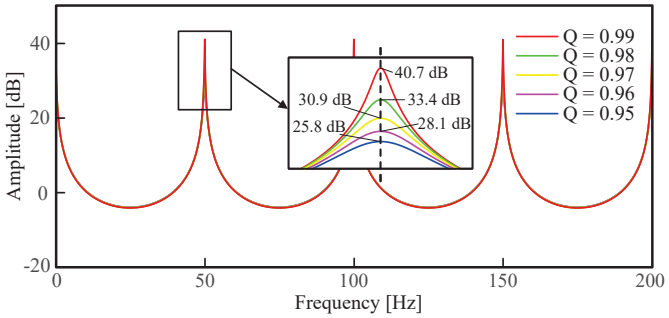

FIGURE 5. Magnitude-frequency curves of repetitive controller with different values of Q.

The compensator $S(z)$ is the most critical component within the repetitive controller. It plays a decisive role in the system stability, error suppression, and tracking accuracy. It typically comprises a control gain, a lead element, and a compensation filter, and can be expressed as follows:

$$S(z) = k_r \cdot z^m S_w(z) \tag{16}$$

where k_r is the control gain; z^m is the lead element; and $S_w(z)$ is the compensation filter.

The complete block diagram of the BIPMSM control system is shown in Fig. 6, with the repetitive controller located within the dashed box. In the diagram, $R(z)$ represents the reference input; $G_p(z)$ represents the controller transfer function; $G_z(z)$ represents the current controller transfer function; $M(z)$ represents the controlled plant; $D(z)$ represents the equivalent disturbance; and $Y(z)$ represents the system output.

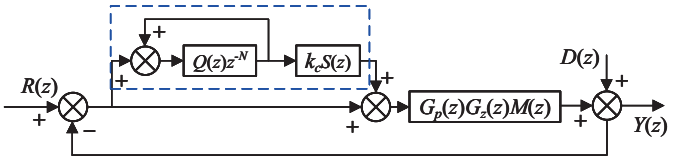

FIGURE 6. Block diagram of the BIPMSM repetitive control system.

The control system transfer function can be written as:

$$\begin{aligned} Y(z) =& \frac{C(z)Q(z)z^{-N}(k_rS(z) - 1) + C(Z)}{1 - Q(z)z^{-N}(1 - k_rS(z)C(z))}R(z) \\ &+ \frac{(1 - Q(z)z^{-N})(1 - C(z))}{1 - Q(z)z^{-N}(1 - k_rS(z)C(z))}D(z) \end{aligned} \tag{17}$$

where $C(z) = G_p(z)G_z(z)M(z)/(1 + G_p(z)G_z(z)M(z))$.

As per the small-gain theorem, for $z = e^{jw}$, the stability condition of the repetitive control system is:

$$|Q(z)(1 - k_rS(z)C(z))| < 1 \tag{18}$$

In (18), the frequency characteristics of $S(z)$ are expressed as $S(jw) = G_s(w)e^{j\varphi s(w)}$, where $G_s(w)$ and $\varphi_s(w)$ are the magnitude-frequency and phase-frequency characteristics of $S(j)$, respectively. Similarly, the frequency characteristics of $C(z)$ are $C(jw) = G_c(w)e^{j\varphi c(w)}$, where $G_c(w)$ and $\varphi_c(w)$ are the magnitude-frequency and phase-frequency characteristics of $C(jw)$, respectively. Substituting $S(jw)$ and $C(jw)$ into (18) and simplifying the derivation reveal that the repetitive control system remains stable when k_c and $(\varphi_s(w) + \varphi_c(w))$ satisfy the following equations:

$$0 < k_r < \frac{-2\cos(\varphi_s(\omega) + \varphi_c(\omega))}{G_s(\omega)G_c(\omega)} \tag{19}$$

$$90° < \varphi_s(\omega) + \varphi_c(\omega) < 270° \tag{20}$$

The compensator is designed with a sampling frequency of 9 kHz. The phase-frequency curve of $C(z)$ is shown in Fig. 7, with a phase range approximately between $-270°$ and $0°$. To satisfy the stability condition in (19) and (20), compensation must be performed separately for low-frequency and high-frequency bands.

In the low-frequency band of the phase-frequency characteristic of $C(z)$, the phase angle is approximately $0°$. Accord-

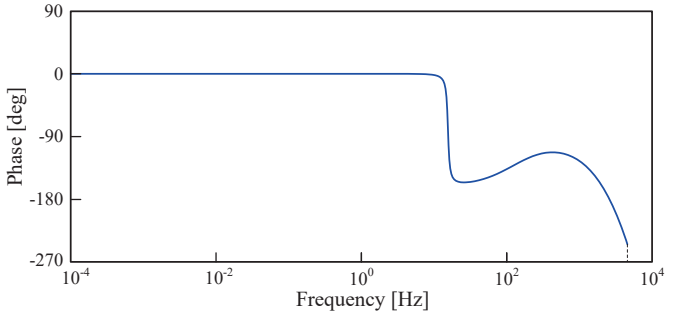

FIGURE 7. Phase-frequency curve of $C(z)$.

ingly, the low-frequency band compensator is designed as follows:

$$S_w(z) = \frac{z - 0.94}{z - 0.01} \tag{21}$$

The phase-frequency characteristic curve after compensation is shown in Fig. 8. The phase angle in the low-frequency band is approximately $180°$, thereby satisfying the stability condition.

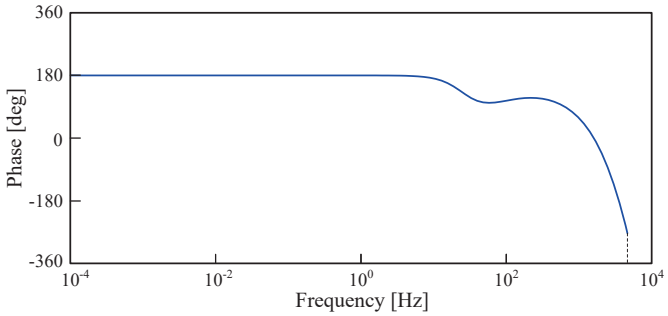

FIGURE 8. Phase-frequency curve of $S_w(z)C(z)$.

The lead element z^m is employed to achieve phase compensation for the high-frequency band. The phase-frequency characteristic curves for m values of 2, 3, and 4 are shown in Fig. 9. Based on the phase stability margin, $m = 3$ is selected. After compensation, the high-frequency band satisfies the stability condition.

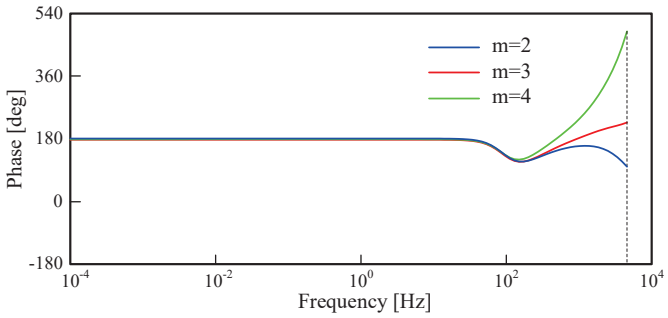

FIGURE 9. Phase-frequency curve of $S_w(z)C(z)z^3$.

Furthermore, according to (19), the stability condition is satisfied when $k_r < 0.96$. In this design, $k_r = 0.9$ is selected. The complete compensator is:

$$S(z) = 0.9z^3 \frac{z - 0.94}{z - 0.01} \tag{22}$$

3.3. Variable Sampling Frequency Method

The operational speed range of the BIPMSM is $[2700, 6000]$ r/min, which indicates that the vibration frequency f_v ranges from 45 to 100 Hz. If a sampling frequency f_s of 10 kHz is assumed, the value of N can only be rounded to the nearest integer when the speed changes, which significantly deteriorates the tracking performance and harmonic suppression capability of the repetitive controller.

This problem is addressed by proposing a repetitive controller based on the variable sampling frequency method, which configures PWM-triggered sampling. The Analog-to-Digital Converter (ADC) is triggered to sample when the PWM signal generates a specific event. The PWM period is dynamically adjusted based on the rotor speed to ensure that the sampling frequency remains a fixed integer multiple N of the fundamental frequency. Additionally, the ADC is configured to generate an interrupt upon the completion of sampling, thereby enabling the processing of sampled data within the interrupt service routine, and the PWM period is continuously updated in a loop. The flowchart of the main function is displayed in Fig. 10.

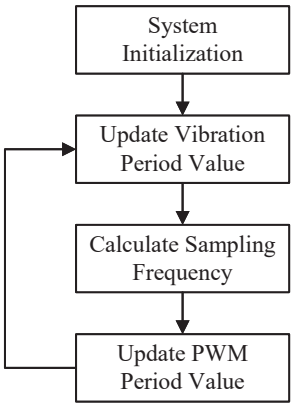

FIGURE 10. Main function flowchart of variable sampling frequency method.

In the experimental BIPMSM platform, the main control chip is TMS320F28335 with a master clock frequency f_{DSP} of 150 MHz. If a value of $N = 200$ is assumed in the repetitive controller, the calculated minimum and maximum sampling frequencies are respectively:

$$\begin{cases} f_{\text{smin}} = f_{v\text{min}} N = 9\,\text{kHz} \\ f_{\text{smax}} = f_{v\text{max}} N = 20\,\text{kHz} \end{cases} \tag{23}$$

As shown in (23), the sampling frequency is 9–20 kHz, which is within the achievable sampling frequency range of the main control chip.

As rounding the PWM period count value introduces certain frequency errors that affect controller accuracy, the resulting error frequency must be analyzed. The PWM period count value ΔP can be expressed as:

$$\Delta P = \frac{f_{\text{DSP}}}{f_v N} - \frac{f_{\text{DSP}}}{(f_v + \Delta f_v)N} \tag{24}$$

where Δf_v is the error frequency.

According to (24), the following can be derived:

$$\Delta f_v \approx \frac{f_v^2 N \Delta P}{f_{\text{DSP}}} \tag{25}$$

According to (25), the error frequency Δf_v is positively correlated with the vibration frequency f_v and the PWM period calculation error ΔP. When $f_v = 100$ Hz, $\Delta P = 0.5$, the error frequency reaches its maximum value, calculated to be approximately 0.0067 Hz. The error introduced by rounding the

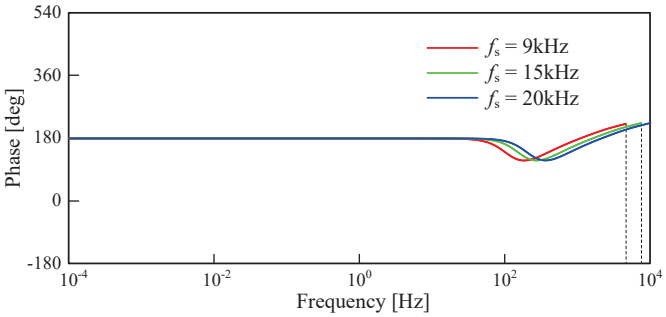

FIGURE 11. Phase-frequency curve of $S_w(z)C(z)z^3$ under multiple sampling frequency.

PWM period count value is negligible, indicating that the sampling frequency can be considered to track the rotor speed with almost no error in a continuous manner.

The repetitive controller is designed at the minimum sampling frequency of 9 kHz. The phase-frequency curves of the compensator are compared under multiple sampling frequencies to verify the stability of the system when the sampling frequency is varied. As shown in Fig. 11, the compensator remains within the stable range across all the tested sampling frequencies; thus, the system stability under different sampling frequencies is validated.

4. SIMULATION AND EXPERIMENT

4.1. Simulation

To verify the effectiveness of the proposed vibration suppression strategy, a model of the repetitive control system for the BIPMSM is built using the Simulink module in MATLAB, and simulations are performed. The topology of BIPMSM is shown in Fig. 12. The parameters of the BIPMSM are listed in Table 1.

TABLE 1. BIPMSM parameters.

Description	Parameters	value
Pole pair number of torque winding	P_T	2
Pole pair number of suspension force winding	P_S	3
Torque winding resistance (Ω)	R_T	1.14
Suspension force winding resistance (Ω)	R_S	1.7
Torque winding d-axis inductance (mH)	L_{Td}	5
Torque winding q-axis inductance (mH)	L_{Tq}	7.8
Suspension force winding inductance (mH)	L_S	9.5
Back EMF of torque winding (V)	E_T	4.99
Back EMF of suspension force winding (V)	E_S	7.5
Rotor mass (kg)	m	1.94
Moment of inertia (kg · m^2)	J	0.0008

Comparative simulations of the proposed vibration suppression strategy and fractional-order delay repetitive controller are conducted at three operating conditions: 3000, 4500, and 6000 r/min. The results are presented in Fig. 13. Compared with the fractional-order delay repetitive controller, the proposed vibration suppression strategy reduces the rotor displacement by 23.5%, 18.2%, and 14.7% in the x-direction, and by 26.7%, 30.2%, and 15.6% in the y-direction at 3000, 4500, and 6000 r/min, respectively. The suspension accuracy of the BIPMSM is significantly improved.

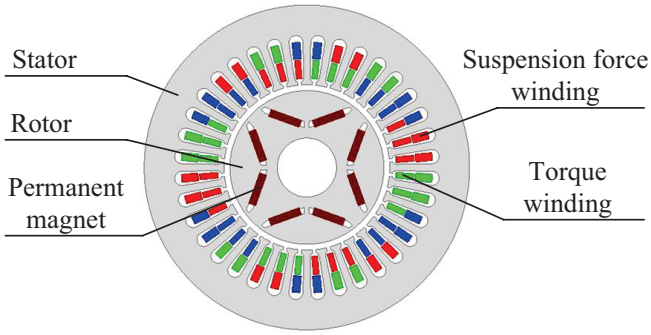

FIGURE 12. Topology of BIPMSM.

Figure 14 depicts the comparative fast Fourier transform (FFT) analysis results of the x-displacement before and after applying the repetitive controller at 3000 r/min. In addition to the fundamental frequency synchronized with the rotational speed, the 6th and 12th harmonic components are effectively suppressed. Thus, the effectiveness of the proposed method is verified.

4.2. Experiment

A digital system experimental platform with TMS320F28335 as its core main control board is developed for the BIPMSM prototype using a modified repetitive control method, as shown in Fig. 15. The platform mainly includes a BIPMSM prototype, a displacement interface circuit, a digital signal processing (DSP) controller minimum system, a DC power supply, an eddy current sensor, a power driver board, an AC power supply, a personal computer, and other components. The BIPMSM is an experimental prototype, in which the suspension performance is investigated only for the radial displacement at one end of the rotor. Therefore, one end of the rotor is fixed by a bearing, while the other end is supported by an auxiliary bearing. A clearance is reserved between the shaft and the auxiliary bearing to allow flexibility in the radial displacement of the rotor while ensuring that the stator and rotor do not come into contact. The prototype parameters remain consistent with those used in the simulation. The block diagram of the digital system structure is shown in Fig. 16.

Comparative experiments are conducted at operating speeds of 3000, 4500, and 6000 r/min under three conditions: without vibration suppression, with the fractional-order delay repetitive controller, and with the variable sampling frequency repetitive controller. After the motor maintains a steady state for 10 s, the rotor radial displacement waveform is continuously acquired. As shown in Fig. 17, the rotor radial displacement increases with the rotational speed and the vibration frequency is synchronized with the rotational speed. Thus, the accuracy of the

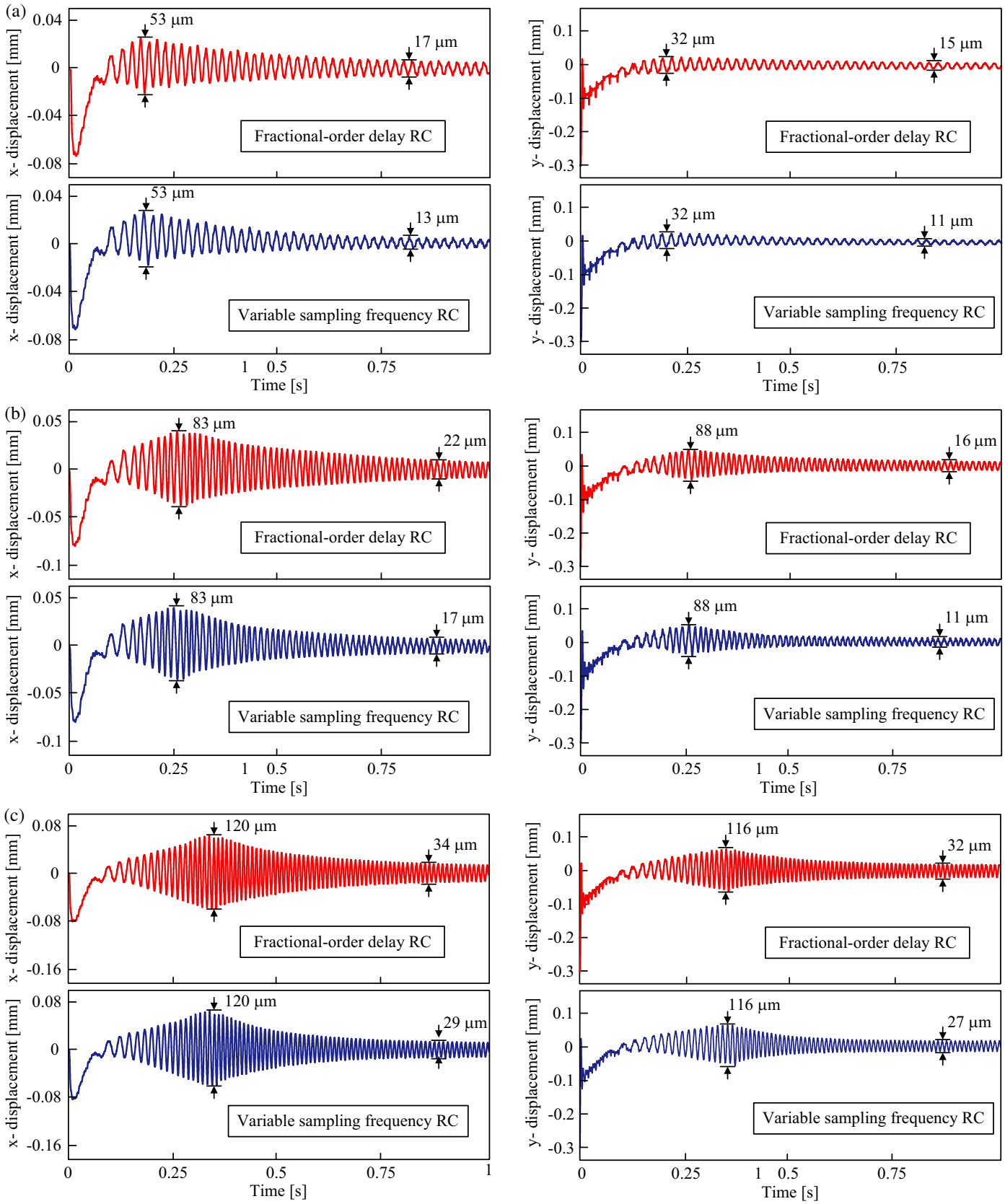

FIGURE 13. Simulation results of radial displacement. (a) 3000 r/min. (b) 4500 r/min. (c) 6000 r/min.

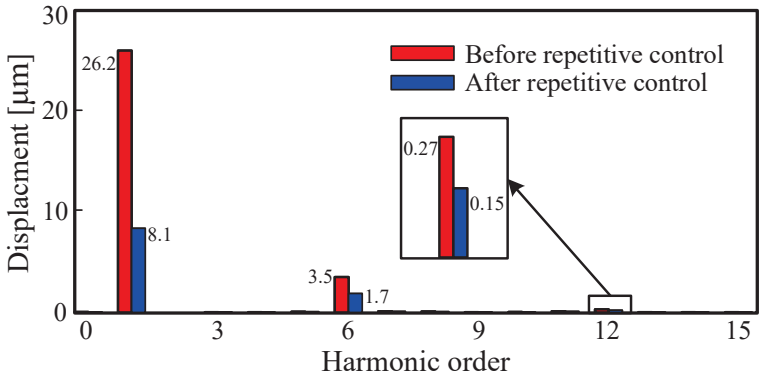

FIGURE 14. Comparative harmonic analysis of x-displacement at 3000 r/min.

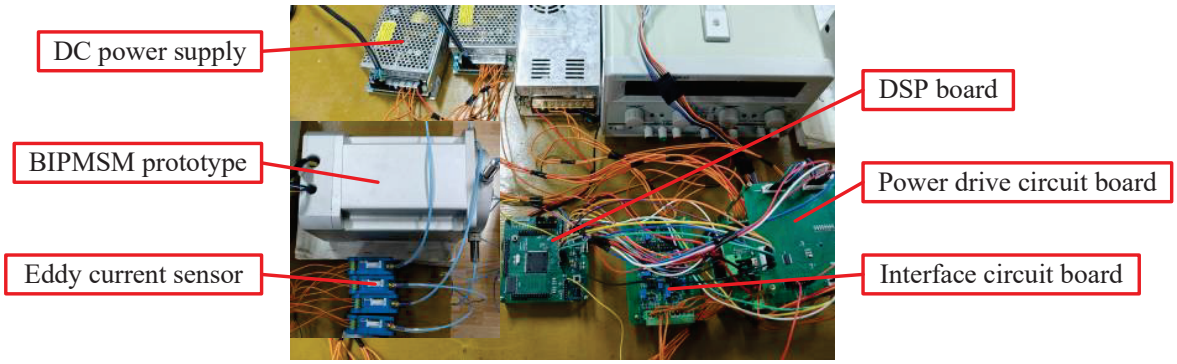

FIGURE 15. Experimental platform.

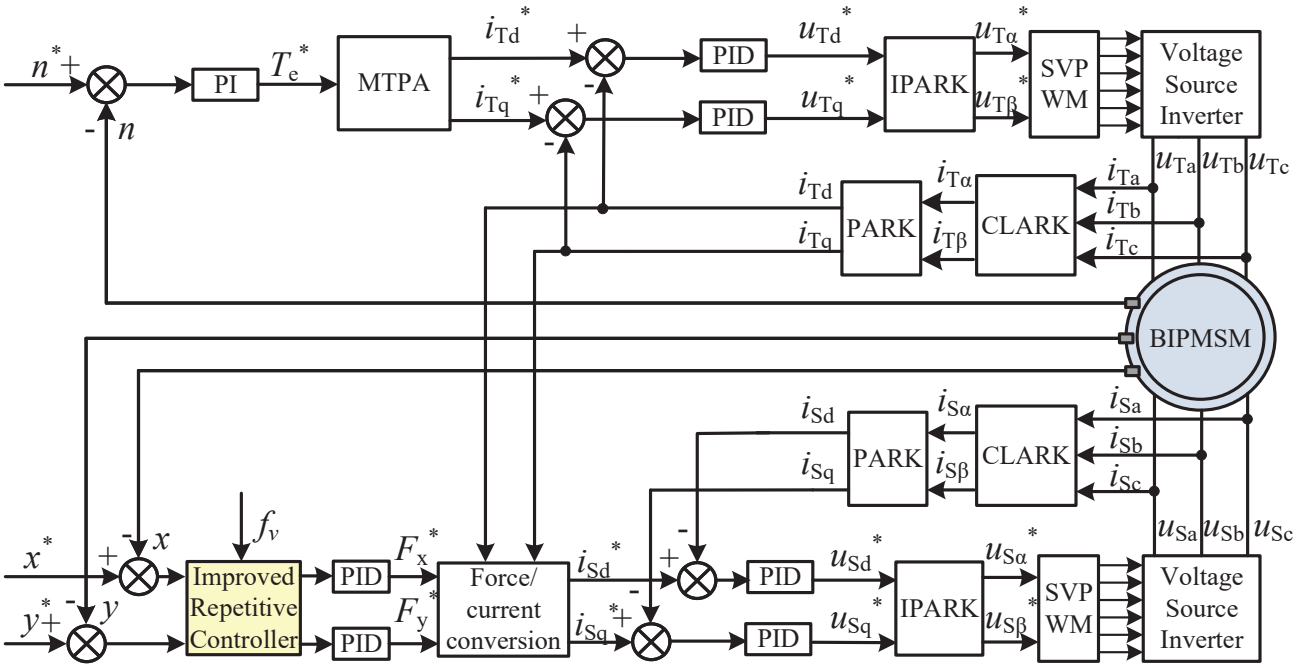

FIGURE 16. Block diagram of the BIPMSM digital system.

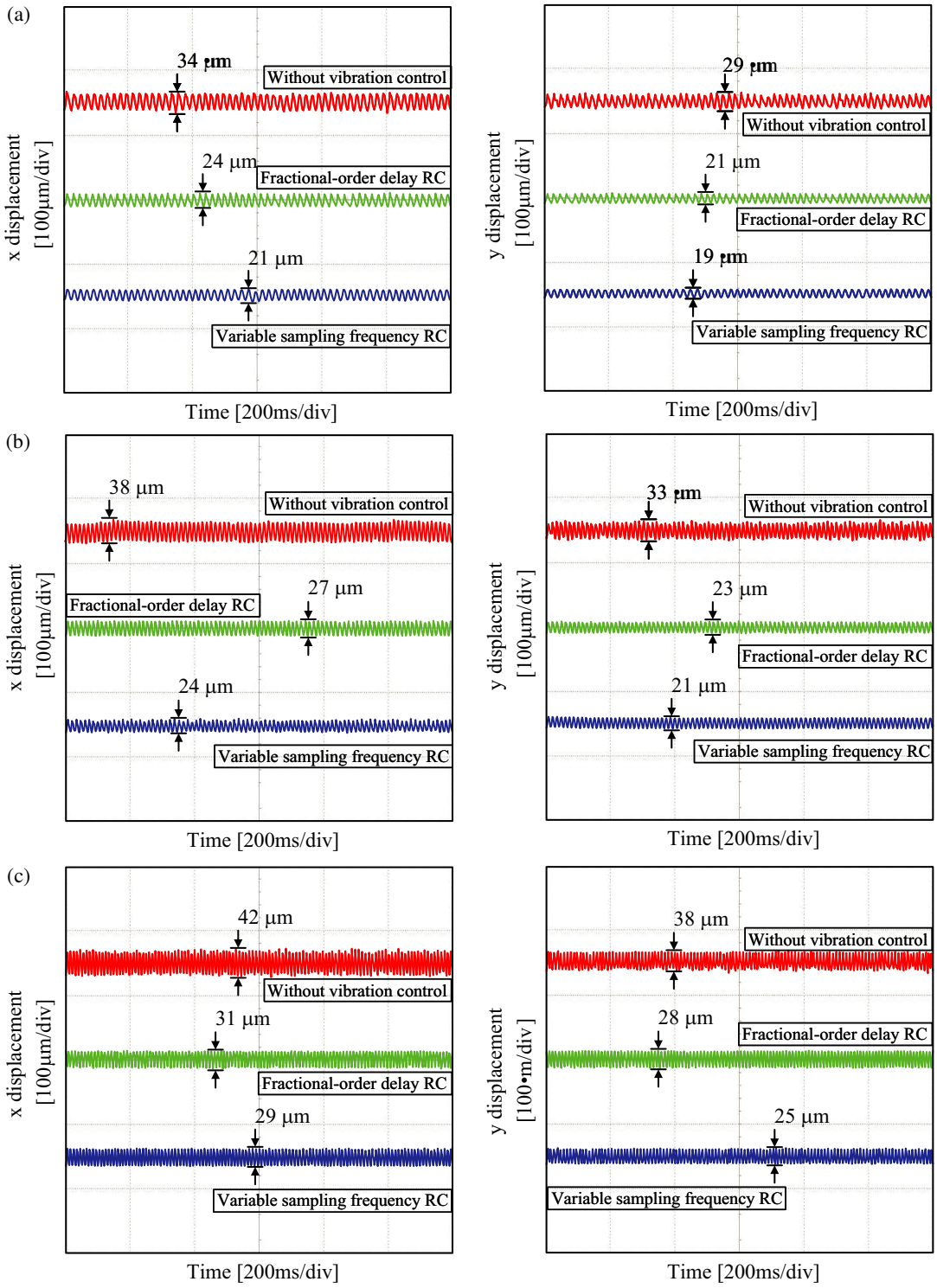

FIGURE 17. Exp erimental results of radial displacement. (a) 3000 r/min. (b) 4500 r/min. (c) 6000 r/min.

vibration mechanism analysis is verified. Under all the operating conditions, both the fractional-order delay and variable sampling frequency repetitive controllers effectively suppress radial rotor vibrations in the BIPMSM. The control performance of the variable sampling frequency repetitive controller is approximately 10% higher than that of the fractional-order delay repetitive controller. The effectiveness of the proposed control strategy is validated.

5. CONCLUSION

In this study, a vibration suppression control strategy utilizing a repetitive controller with a variable-sampling-frequency method is proposed based on the analysis of the rotor vibration mechanism in BIPMSMs. The conclusions are summarized as follows:

1) The rotor vibration mechanism is analyzed in terms of the unbalanced rotor mass and dead-time effect. Furthermore, the

mathematical model of the unbalanced force and rotor vibration frequency is determined.

2) A repetitive controller based on the variable-sampling-frequency method is proposed to enable the stable operation of BIPMSMs over a wide frequency range. When the rotor vibration frequency varies, the order of the repetitive controller N remains constant, exhibiting considerable stability.

3) Simulations and experiments are performed to confirm that the proposed vibration suppression strategy can significantly reduce rotor displacement vibrations, thereby improving the suspension accuracy of BIPMSMs.

Additionally, various nonlinear factors exist within the inverter, such as switching ringing, which will also lead to vibrations in BIPMSMs. Future research will focus on further investigating these nonlinear factors.

ACKNOWLEDGEMENT

This project was sponsored in part by the National Natural Science Foundation of China (62403217) and in part by the Natural Science Foundation of Jiangsu Province (BK20240866).

REFERENCES

[1] Sun, X., L. Chen, and Z. Yang, "Overview of bearingless permanent-magnet synchronous motors," *IEEE Transactions on Industrial Electronics*, Vol. 60, No. 12, 5528–5538, Dec. 2013.

[2] Singh, D. and A. Chiba, "Basic design and analysis results of 800 kW bearingless motor with consequent-pole rotor," in *2025 IEEE Industry Applications Society Annual Meeting (IAS)*, 1–6, Taipei, Taiwan, Jun. 2025.

[3] Zhu, H. and M. Wu, "Direct control of bearingless permanent magnet synchronous motor based on prediction model," *Progress In Electromagnetics Research M*, Vol. 101, 127–138, 2021.

[4] Pei, T., D. Li, J. Liu, J. Li, and W. Kong, "Review of bearingless synchronous motors: Principle and topology," *IEEE Transactions on Transportation Electrification*, Vol. 8, No. 3, 3489–3502, Sep. 2022.

[5] Mao, B. and H. Zhu, "Unbalance vibration suppression control of PMa-BSynRM based on total least square adaptive filtering algorithm," *IEEE Journal of Emerging and Selected Topics in Power Electronics*, Vol. 11, No. 6, 5798–5808, 2023.

[6] Zhu, H., Z. Yang, X. Sun, D. Wang, and X. Chen, "Rotor vibration control of a bearingless induction motor based on unbalanced force feed-forward compensation and current compensation," *IEEE Access*, Vol. 8, 12 988–12 998, 2020.

[7] Lu, J., T. Zhao, and H. Zhu, "Vibration suppression control of PMa-BSynRM based on variable step size and variable angle search algorithm," *Progress In Electromagnetics Research B*, Vol. 113, 77–86, 2025.

[8] Li, Z., X. Wang, and X. Bao, "Full compensation strategy for synchronous vibration suppression of BPMSM," *IEEE Transactions on Industry Applications*, Vol. 62, No. 1, 908–919, 2026.

[9] Peng, C., S. Zheng, Z. Huang, and X. Zhou, "Complete synchronous vibration suppression for a variable-speed magnetically suspended flywheel using phase lead compensation," *IEEE Transactions on Industrial Electronics*, Vol. 65, No. 7, 5837–5846, Jul. 2018.

[10] Zuo, S., H. Wu, Y. Liu, and W. Deng, "Analysis and reduction of electromagnetic noise induced by dead time effect for an axial-flux permanent magnet motor," in *2019 22nd International Conference on Electrical Machines and Systems (ICEMS)*, 1–6, Harbin, China, 2019.

[11] Shahsavari, B., E. Keikha, F. Zhang, and R. Horowitz, "Adaptive repetitive control design with online secondary path modeling and application to bit-patterned media recording," *IEEE Transactions on Magnetics*, Vol. 51, No. 4, 1–8, Apr. 2015.

[12] Chen, Y., C. Zhao, L. Tan, and Z. Zhang, "Harmonic suppression strategy in flux-weakening control of interior permanent magnet synchronous motor using repetitive controllers," in *2021 24th International Conference on Electrical Machines and Systems (ICEMS)*, 1894–1899, Gyeongju, Korea, 2021.

[13] Zou, Z.-X., K. Zhou, Z. Wang, and M. Cheng, "Frequency-adaptive fractional-order repetitive control of shunt active power filters," *IEEE Transactions on Industrial Electronics*, Vol. 62, No. 3, 1659–1668, Mar. 2015.

[14] Chiba, A., T. Fukao, O. Ichikawa, M. Oshima, M. Takemoto, and D. G. Dorrell, *Magnetic Bearings and Bearingless Drives*, Elsevier, 2005.

[15] Wang, X. and H. Zhu, "Vibration compensation control of BPMSM with dead-time effect based on adaptive neural network band-pass filter," *IEEE Transactions on Power Electronics*, Vol. 37, No. 6, 7145–7155, Jun. 2022.

[16] Tang, Z. and B. Akin, "A new LMS algorithm based deadtime compensation method for PMSM FOC drives," *IEEE Transactions on Industry Applications*, Vol. 54, No. 6, 6472–6484, Nov.–Dec. 2018.

[17] Josifović, I., J. Popović-Gerber, and J. A. Ferreira, "Improving SiC JFET switching behavior under influence of circuit parasitics," *IEEE Transactions on Power Electronics*, Vol. 27, No. 8, 3843–3854, Aug. 2012.

[18] Camacho, A. P., V. Sala, H. Ghorbani, and J. L. R. Martinez, "A novel active gate driver for improving SiC MOSFET switching trajectory," *IEEE Transactions on Industrial Electronics*, Vol. 64, No. 11, 9032–9042, Nov. 2017.

[19] Mattavelli, P. and F. P. Marafao, "Repetitive-based control for selective harmonic compensation in active power filters," *IEEE Transactions on Industrial Electronics*, Vol. 51, No. 5, 1018–1024, Oct. 2004.

[20] Ye, X., X. Tang, K. Xing, H. Wang, J. Yao, and T. Zhang, "Repetitive control for vibration suppression of bearingless induction motor," *IEEE Access*, Vol. 12, 60 532–60 540, 2024.